

DTIC FILE COPY

2

AFOSR-TR-88-1141

AD-A199 629

DTIC  
ELECTE  
OCT 11 1988  
S H D



# College of Engineering Iowa State University

DISTRIBUTION STATEMENT A

Approved for public release;

Dist. by the DTIC

REPORT DOCUMENTATION PAGE

1a. REPORT SECURITY CLASSIFICATION Unclassified		b. RESTRICTIVE MARKINGS None	
2a. SECURITY CLASSIFICATION AUTHORITY		DISTRIBUTION/AVAILABILITY OF REPORT Approved for public release; distribution unlimited	
2b. DECLASSIFICATION/DOWNGRADING SCHEDULE None		MONITORING ORGANIZATION REPORT NUMBER(S) <b>AFOSR-TR- 88-1141</b>	
4. PERFORMING ORGANIZATION REPORT NUMBER(S) ISU-ERI-Ames-88175		a. NAME OF MONITORING ORGANIZATION Air Force Office of Scientific Research (AFOSR)	
6a. NAME OF PERFORMING ORGANIZATION Iowa State University Dept. of Mechanical Engineering	6b. OFFICE SYMBOL (if applicable) NA	b. ADDRESS (City, State, and ZIP Code) Air Force Office of Scientific Research Directorate of Aerospace Science (AFOSR/NA) Bolling AFB, DC 20332	
6c. ADDRESS (City, State, and ZIP Code) Room 2025 Black Engineering Ames, IA 50011		7. PROCUREMENT INSTRUMENT IDENTIFICATION NUMBER Grant No. AFOSR-86-0080	
7a. NAME OF FUNDING/SPONSORING ORGANIZATION AFOSR	8b. OFFICE SYMBOL (if applicable) NA	10. SOURCE OF FUNDING NUMBERS	
8c. ADDRESS (City, State, and ZIP Code) Bldg. 410 Bolling AFB, DC 20332-6448		PROGRAM ELEMENT NO. <i>211087</i>	PROJECT NO. <i>1307</i>
		TASK NO. /B1	WORK UNIT ACCESSION NO.
11. TITLE (include Security Classification) Investigation of Liquid Sloshing in Spin-Stabilized Satellites (Unclassified)			
12. PERSONAL AUTHOR(S) Baumgarten, Joseph R.; Prusa, Joseph M.; Flugrad, Donald R.			
13a. TYPE OF REPORT Technical Report	13b. TIME COVERED FROM 87/1/1 TO 87/12/31	14. DATE OF REPORT (Year, Month, Day) 1988 January 31	15. PAGE COUNT i-vii; 1-41
16. SUPPLEMENTARY NOTATION			
17. COSATI CODES		18. SUBJECT TERMS (Continue on reverse if necessary and identify by block number)	
FIELD	GROUP	Coning of satellites, nutation due to sloshing fluid, satellite Attitudes, (yhd) =	
19. ABSTRACT (Continue on reverse if necessary and identify by block number)			
<p>A vorticity, streamfunction approach has resulted in a formulation and numerical algorithm for the two-dimensional viscous sloshing problem. A key feature of the formulation is the use of a coordinate transformation that maps the fluid body into a fixed geometric shape. The formulation also removes an initial singularity from the governing equations that would otherwise cause the numerical method to diverge. An experimental test rig has been designed and built to study the interaction of the sloshing fluid and spinning structure. The test rig has been instrumented to monitor the motion of several rotating configurations. In addition, a computer simulation model of the test rig is presently under development.</p> <p>Keywords:</p>			
20. DISTRIBUTION/AVAILABILITY OF ABSTRACT <input checked="" type="checkbox"/> UNCLASSIFIED/UNLIMITED <input checked="" type="checkbox"/> SAME AS RPT. <input checked="" type="checkbox"/> DTIC USERS		21. ABSTRACT SECURITY CLASSIFICATION Unclassified	
22a. NAME OF RESPONSIBLE INDIVIDUAL <i>Dr. Ames</i>		22b. TELEPHONE (Include Area Code) <i>(202) 767-4937</i>	22c. OFFICE SYMBOL NA

1987 Annual Report  
Grant #AFOSR-86-0080

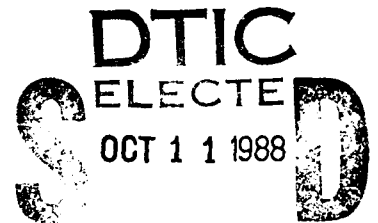
## INVESTIGATION OF LIQUID SLOSHING IN SPIN-STABILIZED SATELLITES

Joseph R. Baumgarten  
Joseph M. Prusa  
Donald R. Flugrad

Department of Mechanical Engineering

January 31, 1988

This report has been prepared for the  
Air Force Office of Scientific Research



# engineering research institute

iowa state university

This is a preprint of a paper intended for publication in a journal or proceedings. Since changes may be made before publication, this preprint is made available with the understanding that it will not be cited or reproduced without the permission of the author.

ISU-ERI Ames 88175  
Project 1873

DISTRIBUTION STATEMENT A

Approved for public release;  
Distribution Unlimited

## TABLE OF CONTENTS

	Page
LIST OF FIGURES	vii
1. INTRODUCTION	1
2. CFD MODEL OF SLOSHING	3
2.1. Formulation of the Two-Dimensional Viscous Model	3
2.1.1. The Governing Equations	3
2.1.2. Initial and Boundary Conditions	6
2.1.3. Coordinate Transformation	7
2.1.4. Nondimensionalization	8
2.1.5. Dimensionless Initial Conditions	13
2.2. The Sloshing Model for an Inviscid Fluid	19
3. TEST RIG DESIGN	23
4. DIMENSIONAL ANALYSIS	35
5. CURRENT STATUS AND FUTURE GOALS	39

Accession For	
NTIS GRA&I	<input checked="" type="checkbox"/>
DTIC TAB	<input type="checkbox"/>
Unannounced	<input type="checkbox"/>
Justification	
By	
Distribution/	
Availability Codes	
Dist	Special
A-1	

## LIST OF FIGURES

	Page
Figure 1. Geometry of the model.	4
Figure 2. Geometry of the six regions.	12
Figure 3. Similarity solution: streamfunction ( $df = 0.025$ ).	16
Figure 4. Similarity solution: pressure.	17
Figure 5. Similarity profiles in boundary layers.	18
Figure 6. Free surface position vs time.	21
Figure 7. RMS deviation from equilibrium position of free surface with time.	22
Figure 8. Photograph of completed test rig, initial design configuration.	24
Figure 9. Coordinate system and Euler angle definitions for STAR 48 test rig.	26
Figure 10. Angular rates vs time for STAR 48, computer simulation.	28
Figure 11. Angular rates vs time for STAR 48, actual telemetered data.	29
Figure 12. Angular rates vs time for the initial test rig design configuration, computer simulation.	30
Figure 13. Angular rates vs time for second test rig design configuration, computer simulation.	32
Figure 14. Photograph of completed test rig, second design configuration, spin about axis of maximum moment of inertia.	33
Figure 15. Present test rig with modified design and instrumentation.	40

## 1. INTRODUCTION

This report outlines the progress of our research effort for 1987 and forecasts the research plans for the first half-year of activity of 1988.

Work on the modeling of the sloshing fluid has resulted in a formulation and numerical algorithm for the two-dimensional viscous sloshing problem. On the basis of our experiences, we have chosen to use a vorticity, streamfunction approach rather than a primitive variable approach because of its inherent mass conservation property. A key feature of the formulation is the use of a coordinate transformation that maps the fluid body into a fixed geometric shape. The formulation also removes an initial singularity from the governing equations that would otherwise cause the numerical method to diverge. Highlights of the formulation as well as some preliminary results are given in the next chapter.

We designed and built an experimental test rig to study the interaction between the sloshing fluid and the spinning structure. Results verified what would be predicted from a classical dynamic model of a rigid, torque-free body. The test rig exhibited unstable motion when spun about an axis of intermediate moment of inertia, but the motion was stable for rotation about an axis of maximum moment of inertia. Details are presented in Chapter 3 of this report. A dimensional analysis was also conducted, to identify the significant parameters associated with the dynamic behavior of such a system. The results are described in Chapter 4.

On the basis of experience with the initial test rig configuration, modifications were incorporated to allow for rotation of the spinning assembly about an axis of minimum moment of inertia. Instrumentation was also added to monitor the motion with a data acquisition system. Currently, the transducers are being calibrated and fine-tuned for test runs scheduled for the near future.

Development of two versions of a computer simulation model of the test rig dynamics is also well under way. Using equivalent pendula to model the sloshing fluid, we will be able to make useful comparisons between predicted behavior and experimental results. Then, when the computational fluid model is sufficiently developed, it will replace the pendula in the simulation.

## 2. CFD MODEL OF SLOSHING

One of the primary goals of this study is to develop a numerical model capable of describing the sloshing motion that occurs within the fuel stores of a STAR 48 Communications Satellite during the perigee phase of its orbit. When the power assist module (PAM) of the spacecraft fires its thruster to establish the desired geosynchronous earth orbit, the fluid within the fuel stores experiences a sudden axial thrust. Understanding the essential physics of the fluid reaction to this sudden thrust is essential in establishing an accurate numerical model. Consequently, a two-dimensional model that significantly simplifies the geometry is used to study the fluid motion that occurs in a partially filled container as a result of the sudden application of an external force. A detailed description of this model as well as some preliminary results are included.

### 2.1. FORMULATION OF THE TWO-DIMENSIONAL VISCOUS MODEL

The model consists of a rectangular container partially filled with an incompressible viscous fluid (see Fig. 1). Initially, the container is stationary and the fluid is in a state of hydrostatic equilibrium. At time  $t = 0^+$ , an external horizontal force is applied to the container such that the container experiences a constant acceleration toward the right. This sudden application of the external force causes a singularity in the governing equations at time  $t = 0^+$ . This singularity is most clearly evident by the instantaneous adjustment of the pressure field (given the assumption of an incompressible fluid) to the newly imposed conditions. In order to model correctly the fluid motion that occurs moments after the application of the external force, one must remove this singularity from the governing equations. This removal is accomplished by the scaling used in nondimensionalizing the governing equations.

#### 2.1.1. The Governing Equations

The mathematical model describing the fluid motion, which is induced as a result of the sudden container acceleration, is obtained through use of first principles of fluid motion. The equations describing the conservation of mass and momentum for the fluid are formulated for a noninertial reference frame that moves along with the container. These equations are subsequently used to obtain the following dimensional equations:

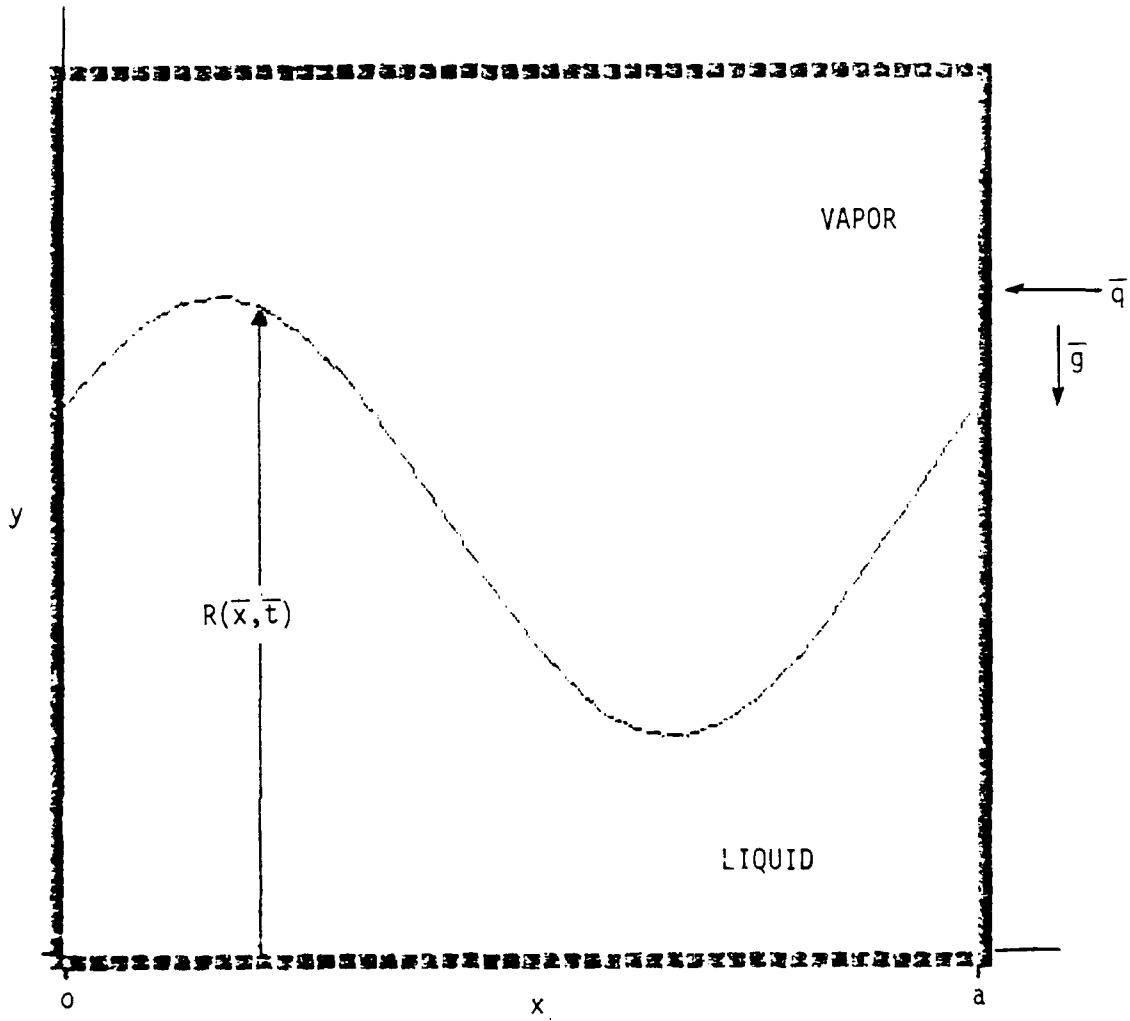


Figure 1. Geometry of the model.

$$\frac{\partial \bar{\omega}}{\partial t} + \frac{\partial(\bar{f}, \bar{\omega})}{\partial(x, y)} = \nu \bar{\nabla}^2 \bar{\omega} \quad (1a)$$

$$\bar{\nabla}^2 \bar{f} = -\bar{\omega} \quad (1b)$$

where

$$\frac{\partial(p, q)}{\partial(x, y)} = \frac{\partial p}{\partial x} \frac{\partial q}{\partial y} - \frac{\partial q}{\partial x} \frac{\partial p}{\partial y} \quad \text{and} \quad \bar{\nabla}^2 = \frac{\partial^2}{\partial x^2} + \frac{\partial^2}{\partial y^2}$$

Equation (1a), the vorticity transport equation, describes the conservation of vorticity. Equation (1b) is the streamfunction Poisson equation, which is obtained by expressing the curl of the velocity vector in terms of the streamfunction. Here, the horizontal and vertical components of velocity are defined in terms of the streamfunction by

$$\bar{u} = -\frac{\partial \bar{f}}{\partial y} \quad \text{and} \quad \bar{v} = \frac{\partial \bar{f}}{\partial x} \quad (2)$$

respectively. The streamfunction-vorticity approach was chosen over the primitive variable approach because of its inherent mass conservation advantage. The pressure variation through the fluid is obtained from the following Poisson equation that is derived by use of the continuity and momentum equations.

$$\nabla^2 \bar{p} = 2\rho \left[ \frac{\partial^2 \bar{f}}{\partial x^2} \frac{\partial^2 \bar{f}}{\partial y^2} - \left( \frac{\partial^2 \bar{f}}{\partial x \partial y} \right)^2 \right] \quad (3)$$

The motion of the free surface is determined from a kinematic condition, which is based upon the assumption that fluid particles on the free surface must remain attached.

$$\frac{\partial R}{\partial t} = \bar{v} - \bar{u} \frac{\partial R}{\partial x} \quad (4)$$

Here,  $R(\bar{x}, t)$  denotes the free surface position with respect to the bottom container wall.

Equations (1a, 1b, and 4) constitute the necessary set of governing differential equations for the

problem. However, completion of the model requires the additional specification of initial and boundary conditions.

### 2.1.2. Initial and Boundary Conditions

The initial conditions at  $t = 0$  are

$$\bar{\omega} \equiv 0 \equiv \bar{f}, \quad R(\bar{x}) \equiv \text{constant}, \quad \text{and} \quad \bar{p} - p_0 = g\rho(R - \bar{y}) \quad (5)$$

where  $p_0$  is the pressure at the free surface.

The following boundary conditions along the container walls are obtained with use of the no-slip condition and momentum conservation at the walls:

for the streamfunction

$$\bar{f} = 0 \quad \text{at} \quad \bar{x} = 0, \bar{x} = a, \text{ and } \bar{y} = 0 \quad (6)$$

for the vorticity

$$\mu \frac{\partial \bar{\omega}}{\partial \bar{x}} = - \frac{\partial \bar{p}}{\partial \bar{y}} - \rho g \quad \text{at} \quad \bar{x} = 0 \text{ and } \bar{x} = a \quad (7)$$

and

$$\mu \frac{\partial \bar{\omega}}{\partial \bar{y}} = \frac{\partial \bar{p}}{\partial \bar{x}} + \rho q \quad \text{at} \quad \bar{y} = 0$$

for the pressure

$$\frac{\partial \bar{p}}{\partial \bar{x}} = - \rho q + \mu \frac{\partial \bar{\omega}}{\partial \bar{y}} \quad \text{at} \quad \bar{x} = 0 \text{ and } \bar{x} = a \quad (8)$$

$$\text{and} \quad \frac{\partial \bar{p}}{\partial \bar{y}} = - \rho g - \mu \frac{\partial \bar{\omega}}{\partial \bar{x}} \quad \text{at} \quad \bar{y} = 0$$

Here,  $\mu$  denotes the fluid viscosity and  $\rho$  the fluid density. The acceleration due to gravity is denoted by  $g$ , while the acceleration experienced by the fluid due to the external force application is denoted by  $q$ . Note that the vorticity and pressure gradients are related by the boundary conditions at the

solid walls. Since the flow is driven by the sudden change in the pressure, it becomes essential that the flow field gets coupled with the pressure field.

One can obtain the boundary conditions at the free surface by requiring that the normal and tangential stresses be continuous across the liquid and vapor interface. Since the free surface is in contact with a much less dense or viscous vapor, one can reasonably assume that stresses on the vapor side are negligible compared with the ones on the liquid side. On the basis of this assumption, the following conditions have to be satisfied at the free surface:

$$\bar{p} - p_o = 2\mu \frac{\partial \bar{u}_n}{\partial n} \quad (\text{normal stress}) \quad (9)$$

$$\frac{\partial \bar{u}_s}{\partial n} + \frac{\partial \bar{u}_n}{\partial s} - \kappa \bar{u}_s = 0 \quad (\text{tangential stress}) \quad (10)$$

where here  $n$  denotes the normal and  $s$  the tangential directions at the free surface. The free-surface curvature is denoted by  $\kappa$ . Equation (9) is used to determine the pressure variation along the free surface, while Eq. (10) is used to obtain the streamfunction variation along the free surface.

### 2.1.3. Coordinate Transformation

One of the difficulties associated with free-surface flow problems is that the shape and position of the free surface are not generally known *a priori*; they are instead determined as part of the solution. This makes the application of boundary conditions at the free surface more difficult and subject to inaccuracies because of irregularities in the shape of the surface. However, these difficulties can be circumvented if a coordinate transformation is introduced that immobilizes the free surface and transforms the irregularly shaped problem domain into a region of a simple regular shape. Consequently, the following coordinate transformation is introduced:

$$x = \frac{\bar{x}}{a} \quad y = \frac{\bar{y}}{R(\bar{x}, \bar{t})} \quad t = \bar{t} / \sqrt{a/g} \quad (11)$$

which immobilizes the free surface and transforms the problem domain into a unit square. The coordinate transformation causes the governing equations to become more complex in form as information pertaining to the shape and motion of the free surface is passed on to the equations through the transformation metrics.

#### 2.1.4. Nondimensionalization

The sudden application of the external force acting on the container at time,  $t = 0^+$ , is transmitted into the fluid by means of a pressure disturbance that originates at the container walls. Since the fluid is being modeled as incompressible, this disturbance is felt throughout the fluid at time  $t = 0^+$ . The pressure field experiences a change in magnitude of order  $O(\rho g)$  while a weak fluid motion of order  $O(qt)$  occurs throughout most of the fluid. The core of the fluid experiences an irrotational, rigid body motion at time  $t = 0^+$ ; while the fluid motion near the container walls is dominated by viscous effects that tend to resist the core motion as fluid particles adjacent to the walls stick to them, forming boundary layers of thickness  $\delta$ . In order to apply the vorticity boundary conditions accurately, the large gradients in the boundary layers must be resolved. To accomplish this, the coordinate normal to each of the container walls is stretched by a factor inversely proportional to the thickness of the boundary layers. The following new coordinate transformations are introduced:

for the core

$$x = \frac{\bar{x} - 2a\delta}{aA}, \quad y = \frac{\bar{y} - a\delta}{a\Gamma} \quad (12)$$

for the left wall boundary layer

$$x^* = \frac{\bar{x}}{a\delta}, \quad y = \frac{\bar{y} - a\delta}{a\Gamma} \quad (13)$$

for the right wall boundary layer

$$x^* = \frac{a - \bar{x}}{a\delta}, \quad y = \frac{\bar{y} - a\delta}{a\Gamma} \quad (14)$$

for the bottom wall boundary layer

$$x = \frac{\bar{x} - 2a\delta}{aA}, \quad y^* = \frac{\bar{y}}{a\delta} \quad (15)$$

where

$$A = (1 - 2\delta), \quad \Gamma = (B - \delta), \quad aB = R, \quad \delta = \sqrt{\eta t} / Ga^{1/4}, \quad Ga = \frac{a^3 g}{\nu^2}$$

Here, the superscript \* indicates a stretched coordinate. More generally, it will be used to refer to any boundary layer variable. The Galileo number, Ga, is a dimensionless group that represents the ratio of gravitational to viscous effects.

In addition to the three major boundary layer regions along each of the container walls, two more regions are created at the lower corners of the container where these boundary layers merge. These are termed the left and right corner layers, and the appropriate coordinate scaling for these regions is given by

for the left corner layer,

$$x^* = \frac{\bar{x}}{a\delta}, \quad y^* = \frac{\bar{y}}{a\delta} \quad (16)$$

for the right corner layer,

$$x^* = \frac{a - \bar{x}}{a\delta}, \quad y^* = \frac{\bar{y}}{a\delta} \quad (17)$$

The nondimensionalization of the dependent variables is determined by scale analysis. The following dimensionless variables result for the core and each of the viscous layers:

for the core

$$f = \frac{\bar{f}}{a^{3/2} g^{1/2} t}, \quad \omega = \frac{a^{1/2} \bar{\omega}}{g^{1/2} t}, \quad p = \frac{\bar{p} - p_o}{\rho a g} \quad (18)$$

for the boundary layers

$$f_i = \frac{\bar{f}}{a^{3/2} g^{1/2} t^{3/2}} \quad \omega_i = \frac{a^{1/2} \bar{\omega}}{g^{1/2} t^{1/2}} \quad p_i = \frac{\bar{p} - p_o}{\rho a g} \quad (19)$$

for  $i = l, r, b, lc, rc$

where the subscripts in Eq. (19) denote the following:  $l$ , a left boundary layer;  $r$ , a right boundary layer;  $b$ , a bottom boundary layer;  $lc$ , a left corner layer; and  $rc$ , right corner layer quantities. When the above coordinate transformations and dimensionless variables are introduced into the governing equations, a set of dimensionless governing equations results for each of the six defined regions (see Fig. 2). The governing equations for the core and the boundary layer along the left wall are given below:

for the core

$$\theta \left( \frac{\partial \phi}{\partial t} + \phi \right) = 2\lambda \frac{\partial \phi}{\partial x} + 2\mu \frac{\partial \phi}{\partial y} + \gamma \frac{\partial^2 \phi}{\partial x^2} + \zeta \frac{\partial^2 \psi}{\partial y^2} + C + S \quad (20)$$

where

$$2\lambda = \left[ \frac{t^2}{A\Gamma} \frac{\partial f}{\partial y} - \frac{\delta}{2A} (1 - 2x) \right] \theta$$

$$2\mu = - \left\{ \frac{t^2}{A\Gamma} \frac{\partial f}{\partial x} - \frac{1}{\Gamma} \left[ yBt + \frac{\delta}{2} (y-1) \right] \right\} \theta + \frac{ty}{A^2Ga^{1/2}} \left[ \frac{2B'^2 - \Gamma B''}{\Gamma^2} \right]$$

$$\gamma = \frac{t}{A^2Ga^{1/2}}, \quad \zeta = \frac{t}{A^2\Gamma^2Ga^{1/2}} (A^2 + y^2B'^2)$$

$$C = - \frac{t}{A^2Ga^{1/2}} \left( \frac{2yB'}{\Gamma} \right) \frac{\partial^2 \phi}{\partial x \partial y}$$

$$S = \begin{cases} 0 \text{ for } \phi = \omega \\ \frac{t\omega}{Ga^{1/2}} \text{ for } \phi = f \\ - \frac{2t^2}{A^2\Gamma^2Ga^{1/2}} \left\{ \frac{\partial^2 f}{\partial y^2} \left[ \frac{\partial^2 f}{\partial x^2} - \left( \frac{2yB'}{\Gamma} \right) \frac{\partial^2 f}{\partial x \partial y} + \left( \frac{2B'^2}{\Gamma^2} - \frac{B''}{\Gamma} \right) y \frac{\partial f}{\partial y} \right. \right. \\ \left. \left. + \left( \frac{yB'}{\Gamma} \right)^2 \frac{\partial^2 f}{\partial y^2} \right] - \left[ \frac{\partial^2 f}{\partial x \partial y} - \frac{B'}{\Gamma} \frac{\partial f}{\partial y} - \frac{yB'}{\Gamma} \frac{\partial^2 f}{\partial y^2} \right]^2 \right\} \text{ for } \phi = p \end{cases}$$

$$\theta = \begin{cases} 1 \text{ for } \phi = \omega \\ 0 \text{ for } \phi = f, p \end{cases} \quad B' = \frac{\partial B}{\partial x}, \quad B'' = \frac{\partial^2 B}{\partial y^2}$$

for the left boundary layer

$$\theta \left( \frac{\partial \phi}{\partial x} + \frac{\phi}{2} \right) = 2\lambda^* \frac{\partial \phi}{\partial x} + 2\mu^* \frac{\partial \phi}{\partial y} + \gamma^* \frac{\partial^2 \phi}{\partial x^2} + \zeta^* \frac{\partial^2 \phi}{\partial y^2} + C^* + S^* \quad (21)$$

where

$$2\lambda^* = \left( \frac{t^2 Ga^{1/4}}{\sqrt{n} \Gamma} \frac{\partial f}{\partial y} + \frac{x^*}{2} \right) \theta$$

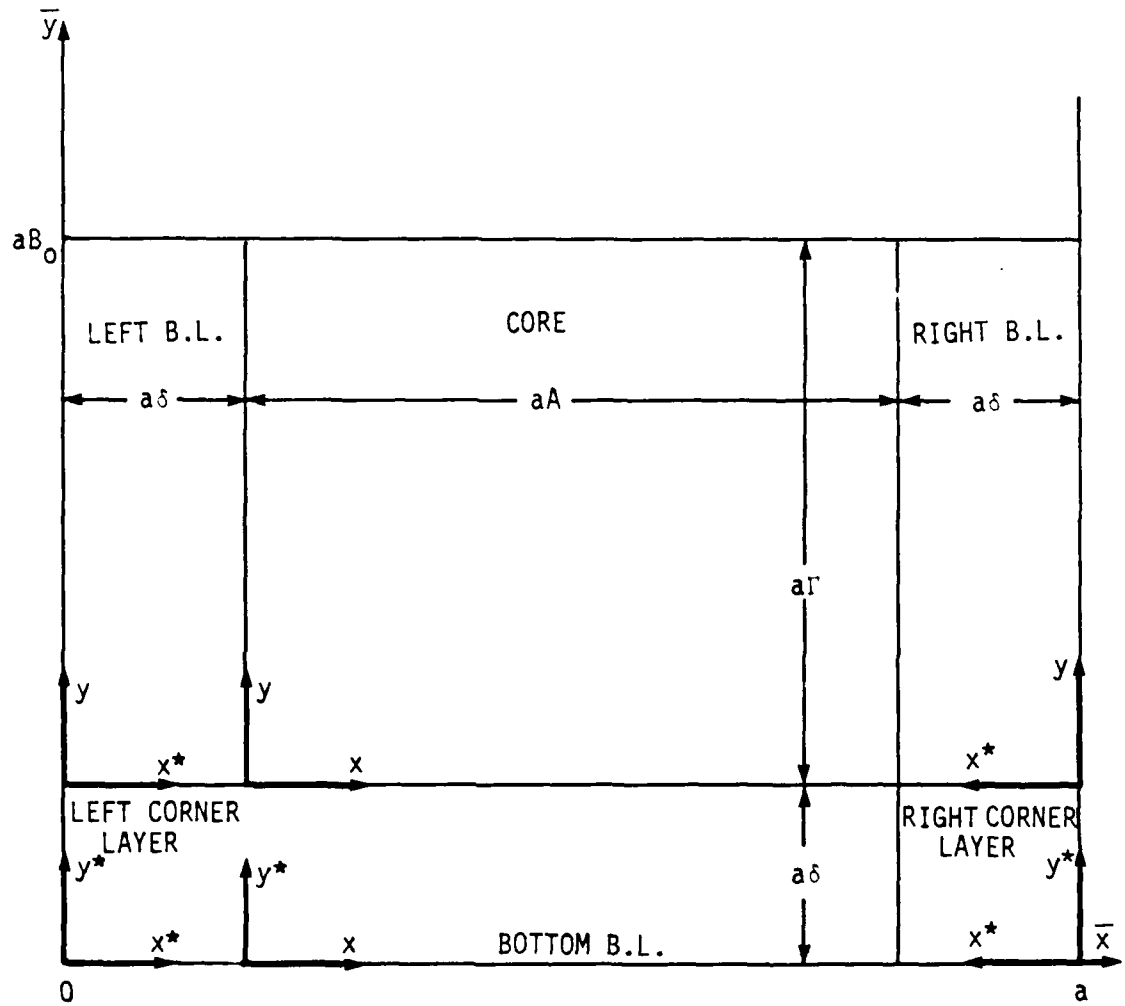


Figure 2. Geometry of the six regions.

$$2\mu^* = - \left\{ \frac{t^2 Ga^{1/4}}{\sqrt{n} \Gamma} \frac{\partial f_\ell}{\partial x^*} - \frac{1}{\Gamma} \left[ y \dot{\Delta} t + \frac{\delta}{2} (y-1) \right] \right\} \theta + \frac{y}{\eta \Gamma^2} (2B'^2 - B''\Gamma)$$

$$\gamma^* = \frac{1}{\eta}, \quad \zeta^* = \frac{1}{\eta \Gamma^2} (\delta^2 + y^2 B'^2), \quad C = - \left( \frac{2yB'}{\eta \Gamma} \right) \frac{\partial^2 \phi}{\partial x^* \partial y}$$

$$S^* = \begin{cases} 0 & \text{for } \phi = \omega_\ell \\ \frac{\omega_\ell}{Ga^{1/2}} & \text{for } \phi = f_\ell \\ - \frac{2t^3}{\eta \Gamma^2} \left\{ \frac{\partial^2 f_\ell}{\partial y^2} \left[ \frac{\partial^2 f_\ell}{\partial x^{*2}} - \left( \frac{2yB'}{\Gamma} \right) \frac{\partial^2 f_\ell}{\partial x^* \partial y} + \left( \frac{2B'^2}{\Gamma^2} - \frac{B''}{\Gamma} \right) y \frac{\partial f_\ell}{\partial y} + \left( \frac{yB'}{\Gamma} \right)^2 \frac{\partial^2 f_\ell}{\partial y^2} \right] \right. \\ \quad \left. - \left[ \frac{\partial^2 f_\ell}{\partial x^* \partial y} - \frac{B'}{\Gamma} \frac{\partial f_\ell}{\partial y} - \frac{yB'}{\Gamma} \frac{\partial^2 f_\ell}{\partial y^2} \right]^2 \right\} & \text{for } \phi = p_\ell \end{cases}$$

$$\theta = \begin{cases} 1 & \text{for } \phi = \omega_\ell \\ 0 & \text{for } \phi = f_\ell, p_\ell \end{cases}$$

The governing equations for the remaining viscous regions are similar in form to Eq. (21). It should be noted that although different scaling parameters are used to obtain the equations for different regions, no terms are neglected in any of these equations. In addition to the boundary conditions stated before, matching conditions have been developed for this coupled system of equations. These conditions consist of matching the value and the normal gradient for each of the dependent variables across common boundaries.

### 2.1.5. Dimensionless Initial Conditions

The initial conditions for each of the six regions can be obtained if the limit of the governing equations at  $t = 0^+$  is considered. This yields the following initial conditions:

for the core,

$$B = B_o, \quad \omega = 0, \quad \frac{\partial^2 f}{\partial x^2} + \frac{1}{B} \frac{\partial^2 f}{\partial y^2} = 0, \quad \frac{\partial^2 p}{\partial x^2} + \frac{1}{B^2} \frac{\partial^2 p}{\partial y^2} = 0 \quad (22)$$

for the boundary layers,

$$\frac{1}{\eta} \frac{\partial^2 \omega_i^*}{\partial z^{*2}} + \frac{1}{2} z^* \frac{\partial \omega_i^*}{\partial z^*} - \frac{1}{2} \omega_i^* = 0 \quad (23)$$

$$\frac{Ga^{1/2}}{\eta} \frac{\partial^2 f_i^*}{\partial z^{*2}} = -\omega_i^*$$

where  $z^*$  represents the stretched boundary layer coordinate normal to each wall. The equations for the corner layers are not given since the solution to these equations at  $t = 0^+$  is trivial. The corner layers are characterized by constant pressure and zero streamfunction and vorticity values as no flow occurs in the corner region at  $t = 0^+$  because of friction with the walls. The above initial conditions are subject to the limiting form of the boundary and matching conditions as  $t \rightarrow 0^+$ . The flow in the core is directly driven by the pressure distribution. This is evident from the limiting form of the momentum equations which at time  $t = 0^+$  become

$$u = -\frac{\partial p}{\partial x} - Q \quad \text{and} \quad v = -\frac{1}{B} \frac{\partial p}{\partial y} - 1 \quad (24)$$

Using Eq. (24) and the matching conditions, we can determine the pressure and streamfunction distribution in the core analytically (and independently of the flow in the boundary layers). The core solution at  $t = 0^+$  is given by

$$\omega = 0 \quad (25)$$

$$f(x,y) = \sum_{n=0}^{\infty} b_n \sin[(2n+1)\pi x] \sinh[(2n+1)\pi By] \quad (26)$$

$$p(x,y) = B(1-y) + Q(1/2-x) - \sum_{n=0}^{\infty} b_n \cos[(2n+1)\pi x] \cosh[(2n+1)\pi By] \quad (27)$$

where

$$b_n = \frac{4Q}{\pi^2(2n+1)^2 \cosh[(2n+1)\pi B]} \quad (28)$$

A similarity solution can be obtained for the boundary layers. The general solution of the boundary layer equations can be expressed in terms of the complimentary error function as

$$\omega_i^*(z^*) = C(x,y) \left[ \frac{1}{\sqrt{\pi}} e^{-\frac{\eta z^{*2}}{4}} - \frac{\sqrt{\eta} z^*}{2} \operatorname{erfc}\left(\frac{\sqrt{\eta} z^*}{2}\right) \right] \quad (29)$$

$$f_i^*(z^*) = \frac{C(x,y)}{Ga^{1/2}} \left[ \frac{2}{3\sqrt{\pi}} - \frac{\sqrt{\eta} z^*}{2} + \frac{\sqrt{\eta} z^*}{12} (\eta z^{*2} + 6) \operatorname{erfc}\left(\frac{\sqrt{\eta} z^*}{2}\right) - \left(\frac{\eta z^{*2} + 4}{6\sqrt{\pi}}\right) e^{-\eta z^{*2}/4} \right] \quad (30)$$

where  $C(x,y)$  represents a constant for the boundary layer equations and is determined by matching with the core along the common boundaries.

The initial conditions are also depicted graphically in Figs. 3, 4, and 5. Figure 3 is a plot of lines of constant streamfunction. Note that a clockwise flow occurs from the right to the left container wall. The closer the spacing between lines in the vertical direction, the larger the magnitude of the horizontal velocity component. Similarly, the closer the spacing between the lines in the horizontal direction, the larger the magnitude of the vertical component of the velocity. Consequently, the larger values of velocity occur near the free surface, with the largest vertical component values occurring near the container walls. The value of the horizontal component of velocity along the free surface at  $t = 0^+$  is  $-qt$ . Note, however, that the horizontal velocity component is referenced on a frame moving with the container; thus, in terms of a stationary frame of reference, the stronger flow occurs near the walls. Figure 4 is a plot of lines of constant pressure. Higher pressure values are present in the left half of the container than in the right half, indicating that the free surface will be forced to rise along the left half and fall along the right half of the container. The similarity solution for the flow in the boundary layers is shown in Fig. 5. The streamfunction, and its first and second derivatives with respect to the boundary layer coordinate,  $z^*$ , are plotted. In Fig. 5,  $f_{z^*}^*$  is proportional to the vertical velocity component in the left boundary layer, to the negative of the vertical velocity component in the right boundary layer, and to the negative of the horizontal velocity

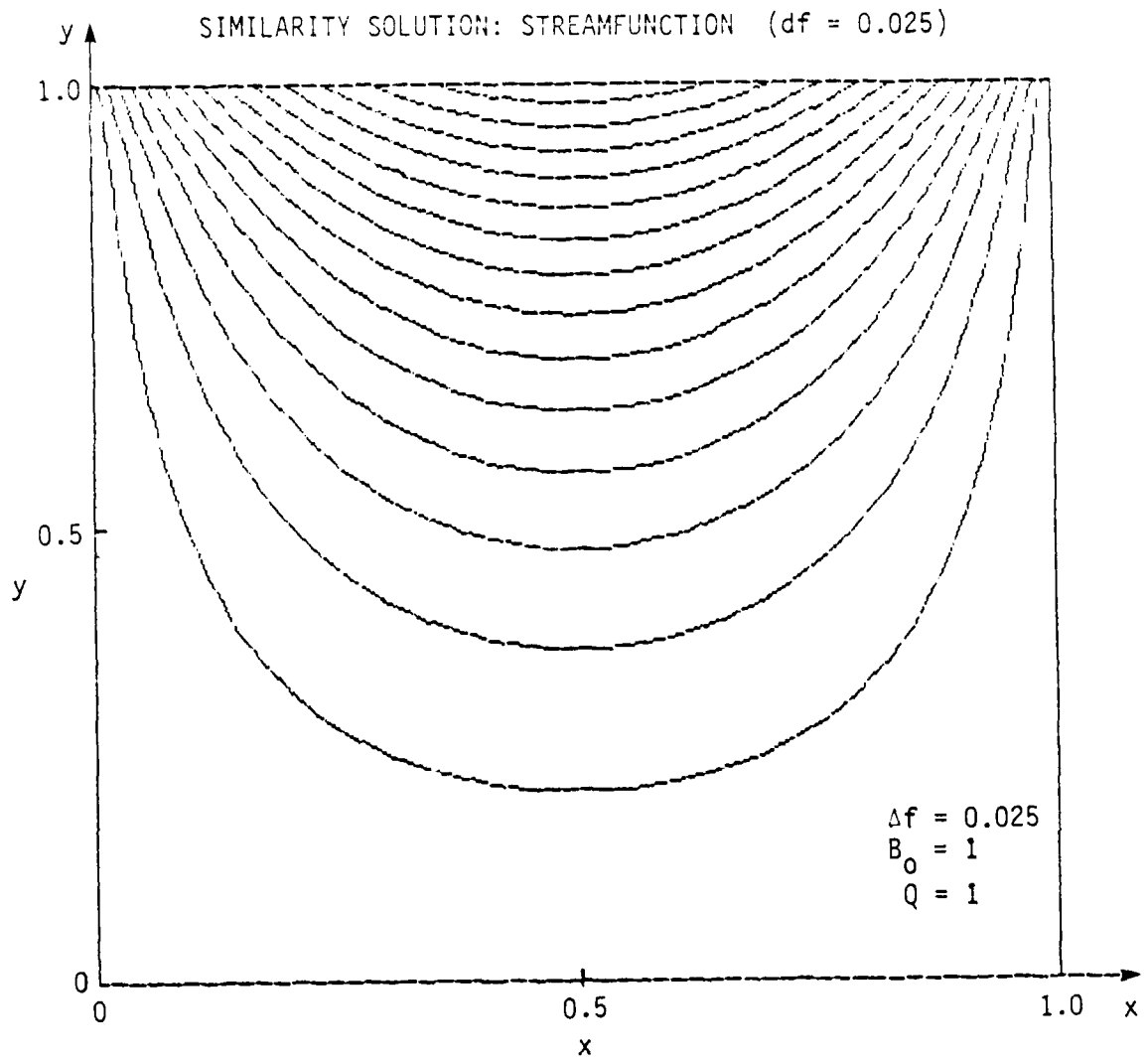


Figure 3. Similarity solution: streamfunction ( $df = 0.025$ ).

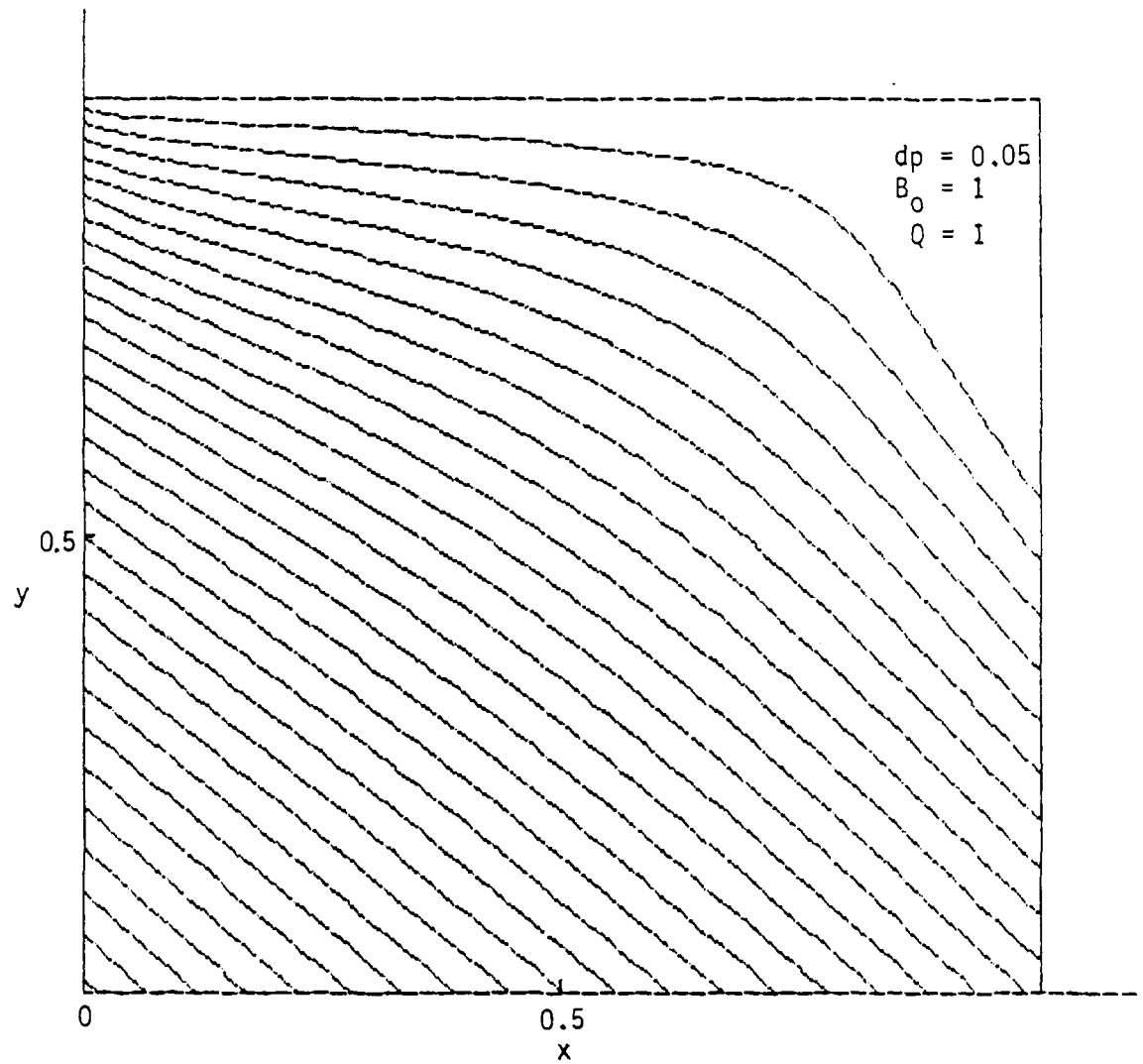


Figure 4. Similarity solution: pressure.

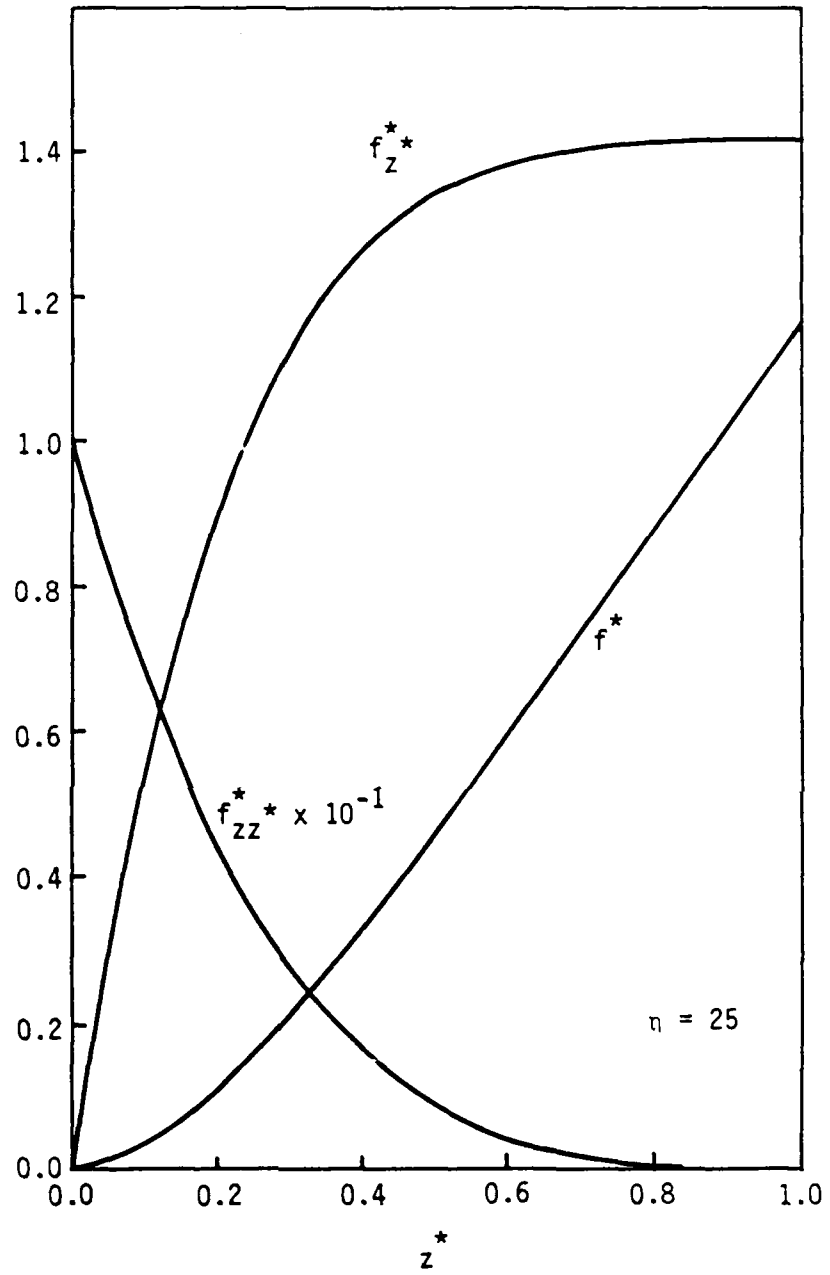


Figure 5. Similarity profiles in boundary layers.

component in the bottom boundary layer. The vorticity in each of the three boundary layers is proportional to  $-f_{zz}^*$ . Note that the maximum vorticity value occurs at the wall, and its magnitude decreases sharply to reach a zero value at the edge of the boundary layer.

## 2.2. The Sloshing Model for an Inviscid Fluid

In the limiting case, as  $Ga \rightarrow \infty$ , the fluid within the container can be treated as inviscid. This greatly simplifies the model because in the absence of any viscous effects, the need for special treatment of regions adjacent to the container walls no longer exists. The viscous boundary conditions at the walls are replaced to allow for slip, and the stress conditions at the free surface are replaced by a conservation of tangential momentum requirement. The resulting irrotational flow can be described by the solution of a Poisson equation for the streamfunction, coupled with the kinematic condition describing the free surface movement. The solution of a Poisson equation for the pressure becomes optional because the flow field is no longer directly coupled with the pressure field.

The flowfield obtained from this model is not expected to differ significantly from the one that will result from the full viscous model for small values of time. This can be expected because for small values of time the viscous effects are predominantly confined next to the container walls. In the absence of any viscous dissipation, the fluid will continuously oscillate about the equilibrium position. However, as time advances, in the presence of viscous dissipation the oscillations will damp out and the fluid will come to rest in a state of hydrostatic equilibrium corresponding to a net acceleration due to gravity and the external force. The position of the free surface at equilibrium is given by

$$B_{eq}(x) = B_o + Q(\frac{1}{2} - x) \quad (31)$$

Figures 6 and 7 show the transient behavior of the free surface for the case with  $B_o = 0.5$  and  $Q = 0.2$ . This corresponds to a square container that is half filled with a fluid experiencing an external force equivalent to 0.2 g. Figure 6 shows the position of the free surface at four different values of time. In Fig. 6a the initial position of the free surface is shown with the solid line, while the dashed line represents the new equilibrium position for the free surface. At time  $t = 1.80$ , the inertia of the fluid has carried it almost to the maximum height that it will reach along the left container wall. The fluid begins to descend along the left wall, passing through the equilibrium position at approximately  $t = 2.85$ , and reaches a position close to its initial distribution by  $t = 3.90$ . Note that the shape of the free surface is no longer flat. It is suspected that this behavior is caused by a nonlinear interaction between the various frequency components of the disturbance at the walls. Figure 7 depicts the

continuous departure of the fluid from the equilibrium position. A root mean square measure of this departure defined by

$$Drms = \frac{\sqrt{12}}{Q^2} \left| \int_0^1 (B(x,t) - B_{eq}(x))^2 dx \right|^{1/2} \quad (32)$$

is plotted versus time. The peaks that appear in Fig. 7 represent the extreme departure positions from equilibrium that are reached when the fluid rises to a maximum or falls to a minimum height along the left wall. The sharply shaped valleys are reached as the fluid passes through the equilibrium position. The sloshing motion exhibits a period of approximately 3.75.

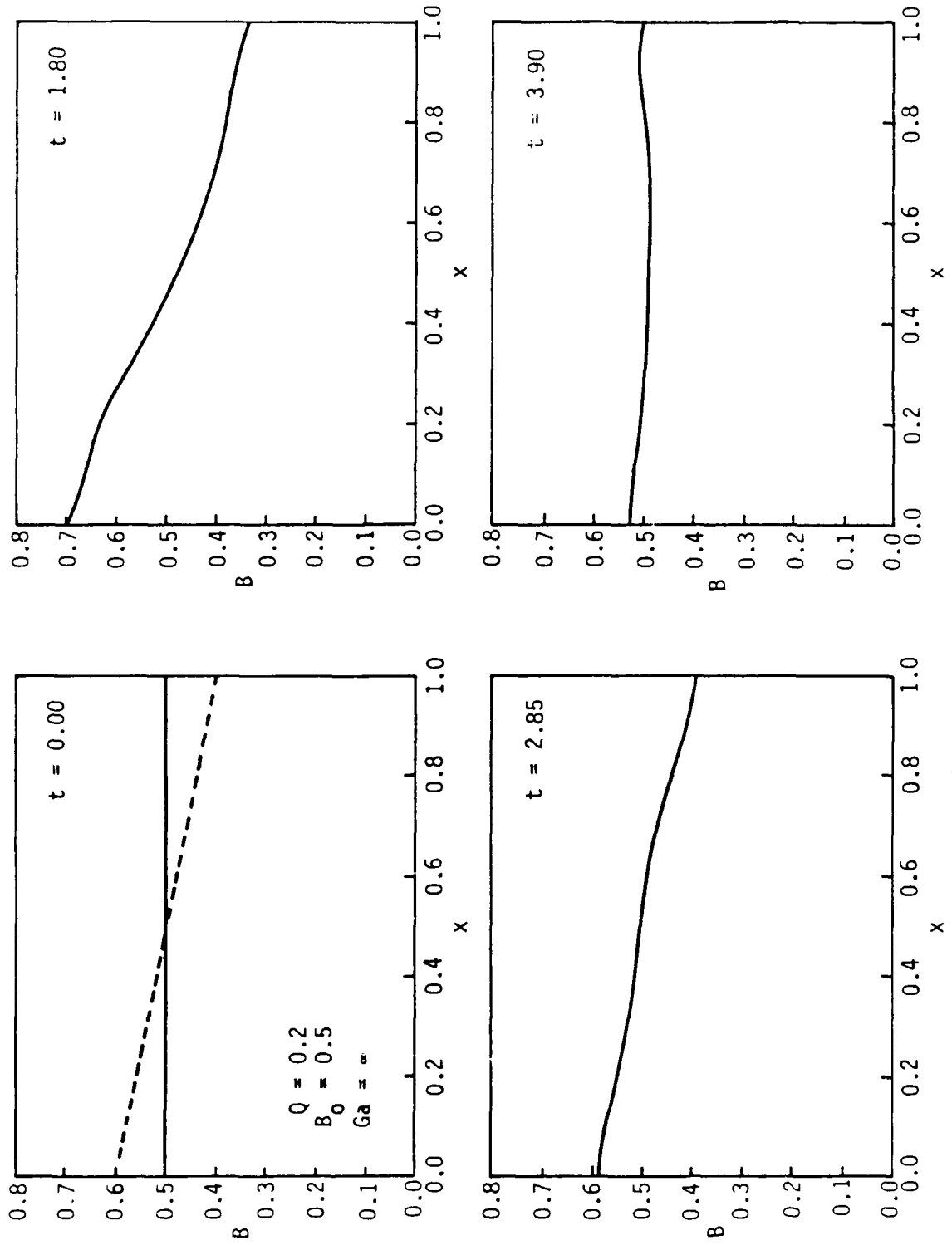


Figure 6. Free surface position vs time.

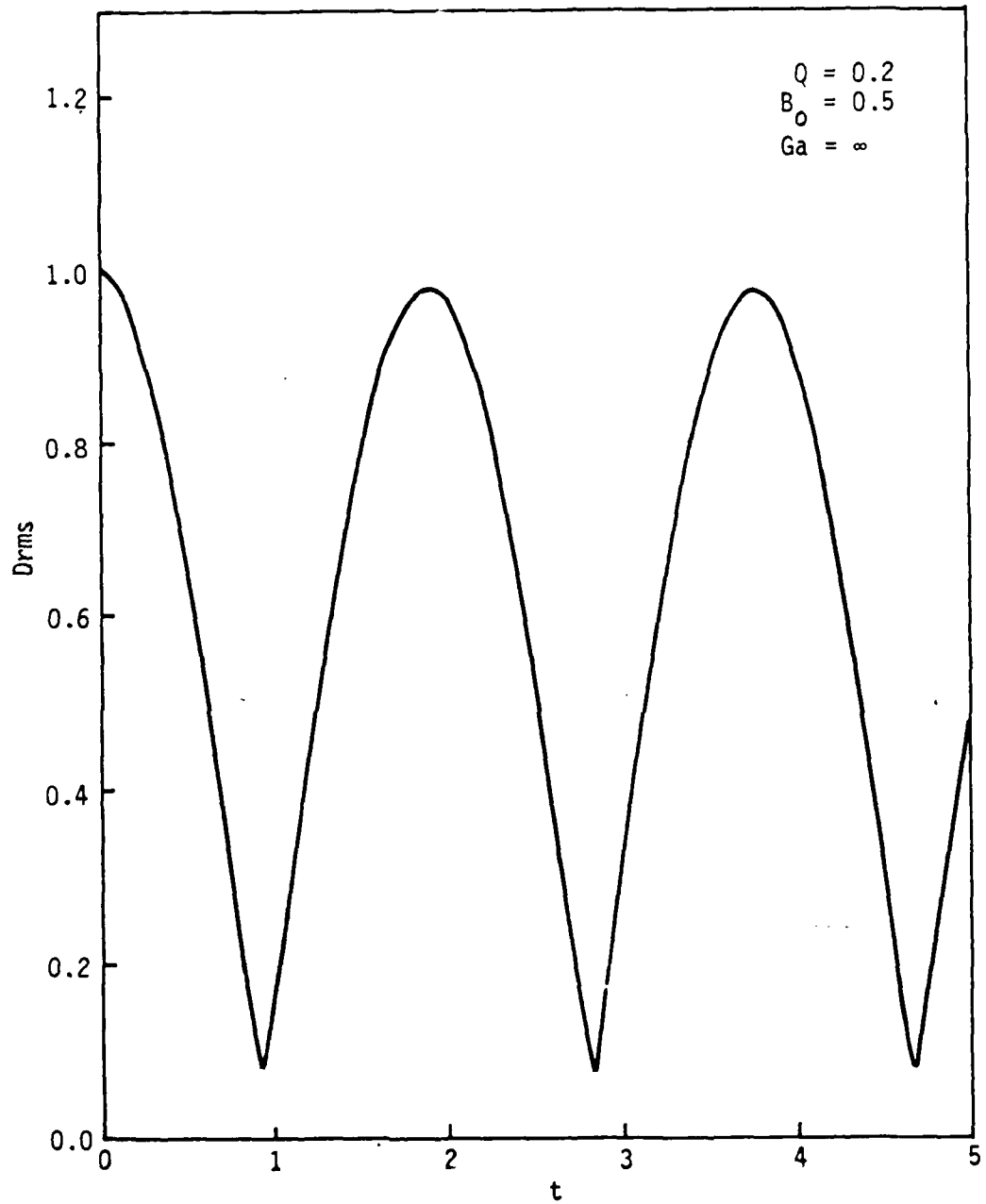


Figure 7. RMS deviation from equilibrium position of free surface with time.

### 3. TEST RIG DESIGN

One phase of the project was to design a physical model to study the effects of sloshing liquid fuel on the stability of a spin-stabilized dynamic system. The design had to allow for modification of most major dimensions to permit the testing of various sizes of tanks and geometric configurations. It was decided that a minimum of instrumentation would be implemented until the operation of the system was better understood so that decisions could be made about which parameters to instrument.

A physical system was conceived that consists of a vertical spin shaft with a horizontal crossbar. Two plastic spheres are supported by the horizontal bar at equal radial distances from the vertical spin axis. A two-degree-of-freedom Hooke's type universal joint is located just below the horizontal beam in the vertical shaft to allow the spin axis of the horizontal beam structure to cone. A yoked sleeve, hand-actuated by a straight-line-motion, 4-bar mechanism is utilized to cover the universal joint to give initial stability and bending rigidity to the system during spin-up. A 1/4 hp electric d.c. motor is the system's prime mover.

Initially, we wanted to design the system to have a first-mode natural frequency of oscillation of 0.5 cycles per second. However, sizing of the spheres from the experimental results of other researchers indicated that large spheres would be required, including a large mass of sloshing fluid. A compromise was achieved by an increase in the natural frequency of the system by a factor of five to 2.5 Hz. This allowed the use of readily available, 6-in.-diameter spheres at a fill height of approximately 3.9 in. The total weight of one of the sphere structures, and hence the beam end load, is approximately five lb.

The sphere-supporting crossbar was analyzed as a non-spinning, continuous-mass, cantilever beam with an end load. Solving the frequency equation for the length of beam resulted in a steel beam 27.32 in. long, 0.625 in. wide, and 0.25 in. thick, with a 5.3-lb. end mass. Overall crossbar length is 54.64 in.

An inertial analysis was performed to determine whether or not a 1/4 hp motor could power the system adequately. We decided to insert a 10:1 gear reducer after the motor to utilize the higher torque capability of the upper speed range of the motor. Since the STAR 48 satellites are spin-stabilized at one revolution per second, this was chosen as the design speed, although speeds up to three times this are possible with the motor and gear reducer system.

A right-angle gear drive connects the horizontal output of the gear reducer to the vertical shaft and pillow block assembly. The vertical shaft diameter was oversized to accommodate pillow block assemblies that were available, as well as to allow for the up-scaling of future configurations.

Figure 8 shows a photograph of the completed assembly prior to any test runs. Note that the spheres were dropped below the center line of the supporting beam in an effort to locate the system center of mass at the intersection of the two universal joint axes.

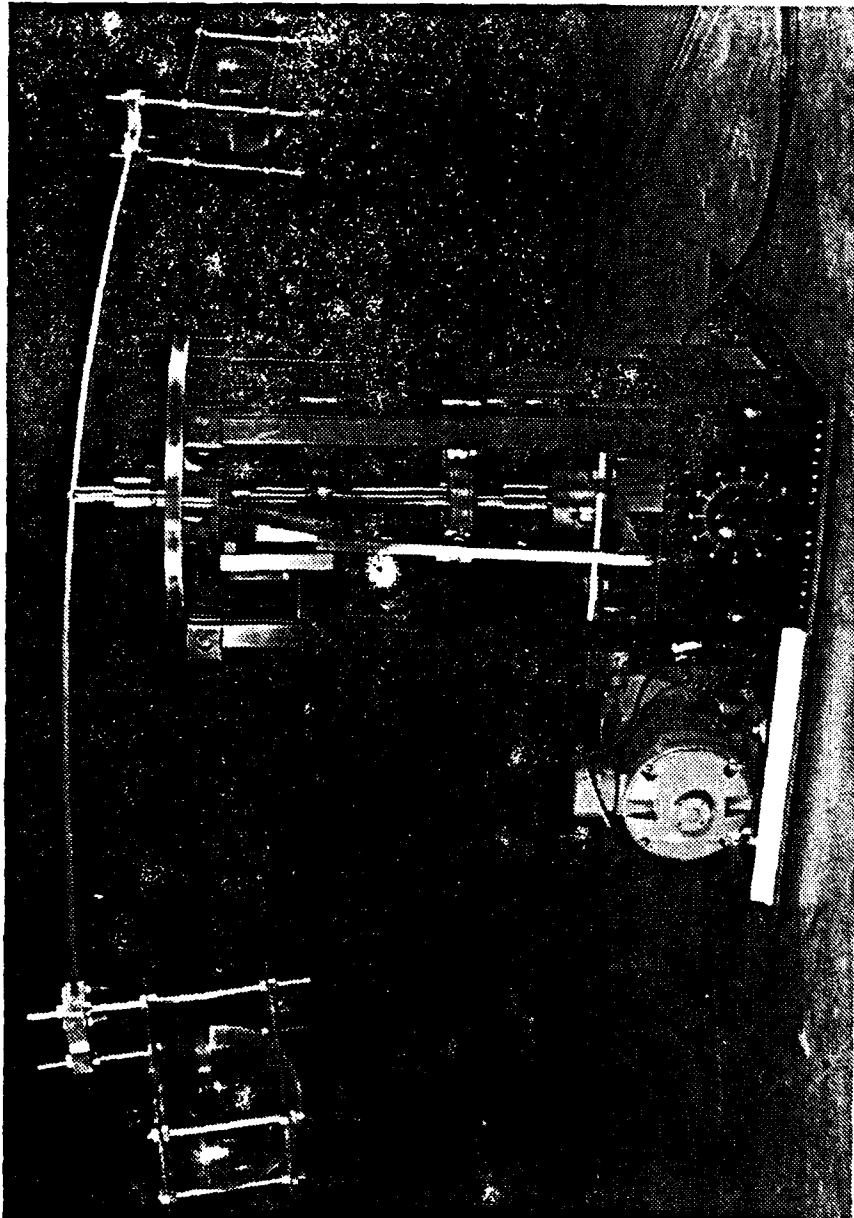


Figure 8. Photograph of completed test rig, initial design configuration.

Operation of the initial design of the completed test rig resulted in a very unstable motion. As soon as the supporting sleeve was lowered, the upper assembly would instantly flop over about an axis parallel to the supporting beam.

An inertial analysis of the system indicated that the spin axis was the intermediate axis of inertia. It is well known that spin of a torque-free, rigid body about its axis of intermediate moment of inertia is an unstable motion. Although the test rig is not rigid, it is assumed to be nearly so and torque-free since the system center of mass is approximately located at the intersection of the universal joint axes.

The differential equations for the rotational motion of a rigid body can be formulated through the use of Lagrange's equations. But the first integrals of the differential equations of motion can be found more directly in the following manner.

A fixed, inertial coordinate system, XYZ, located at the system center of mass was chosen, as shown in Fig. 9, where the support beam is parallel to the X-axis and the Z-axis is vertical. Any new body-fixed coordinate system orientation, xyz, relative to the inertial system, XYZ, can be reached by a series of three rotations about the body axes, performed in the proper sequence. The Euler angles  $\psi$ ,  $\theta$ , and  $\phi$ , which define these three rotations, are presented here in sequence.

1. A positive rotation  $\psi$  about the Z axis, resulting in the primed system in Fig. 9.
2. A positive rotation  $\theta$  about the  $y'$  axis, resulting in the double-primed system in Fig. 9.
3. A positive rotation  $\phi$  about the  $x''$  axis, resulting in the final unprimed system, xyz, in Fig. 9.

When the orthogonal projections of the Euler angle rate vectors onto each of the axes of the xyz coordinate system are determined, expressions for the body axis components of the absolute rotation rate of the body may be written as

$$\begin{aligned}\omega_x &= \dot{\phi} - \dot{\psi} \sin\theta \\ \omega_y &= \dot{\theta} \cos\phi + \dot{\psi} \cos\theta \sin\phi \\ \omega_z &= \dot{\psi} \cos\theta \cos\phi - \dot{\theta} \sin\phi\end{aligned}\tag{33}$$

During initial startup, the test rig is spun about a vertical axis; hence, its momentum vector,  $\mathbf{H}$ , will be vertical. Furthermore, under the assumptions of a torque-free system,  $\mathbf{H}$  will remain vertical after the supporting sleeve is lowered and the assembly is free to exhibit more complex spatial motion. If the angular rate vector of  $\psi$  is chosen to point in a direction opposite the angular momentum,  $\mathbf{H}$ , the body-fixed components of the angular momentum are found from the projections of  $\mathbf{H}$  onto the xyz axes:

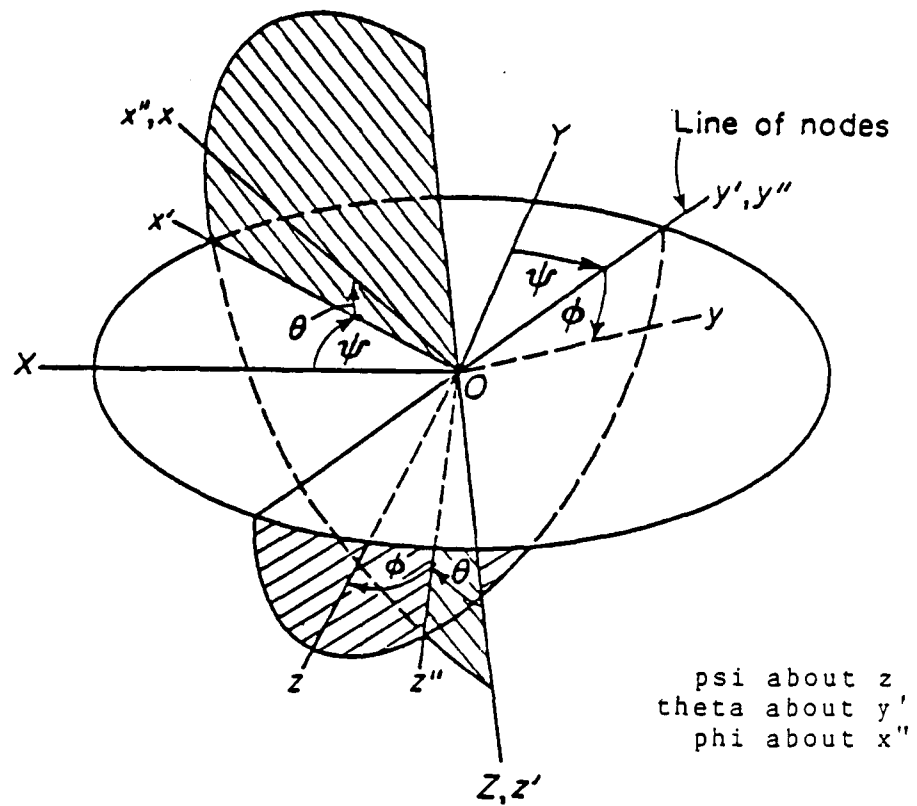


Figure 9. Coordinate system and Euler angle definitions for STAR 48 test rig.

$$\begin{aligned}
 H_x &= I_{xx} \omega_x = H \sin \theta \\
 H_y &= I_{yy} \omega_y = -H \cos \theta \sin \phi \\
 H_z &= I_{zz} \omega_z = -H \cos \theta \cos \phi
 \end{aligned} \tag{34}$$

All products of inertia are zero for the coordinate system chosen, since two of the three coordinate planes are planes of symmetry. Substitution of Eqs. (33) into Eqs. (34) produces

$$\begin{aligned}
 -\dot{\psi} \sin \theta + \dot{\phi} &= (H/I_{xx}) \sin \theta \\
 \dot{\psi} \cos \theta \sin \phi + \dot{\theta} \cos \phi &= (-H/I_{yy}) \cos \theta \sin \phi \\
 \dot{\psi} \cos \theta \cos \phi - \dot{\theta} \sin \phi &= (-H/I_{zz}) \cos \theta \cos \phi
 \end{aligned} \tag{35}$$

Rearranging and solving for the angular rates, one finds

$$\begin{aligned}
 \dot{\psi} &= -H(\sin^2 \phi / I_{yy} + \cos^2 \phi / I_{zz}) \\
 \dot{\theta} &= H(1/I_{zz} - 1/I_{yy}) \cos \theta \sin \phi \cos \phi \\
 \dot{\phi} &= H(1/I_{xx} - \sin^2 \phi / I_{yy} - \cos^2 \phi / I_{zz}) \sin \theta
 \end{aligned} \tag{36}$$

These represent the differential equations of motion in terms of the Euler angle rates.

Software was developed to integrate the equations numerically. A fourth-order Runge-Kutta routine was utilized as provided by subroutine RKGS, a subroutine originally part of the SSP subroutine package developed by IBM. Angular rates were then plotted versus time.

To verify the proper operation of the simulation software, we simulated the rigid body dynamics of a STAR 48 satellite by utilizing actual inertial characteristics of a STAR 48 after PAM motor burnout, where  $I_x = 606$ ,  $I_y = 606$ , and  $I_z = 318$  slug ft<sup>2</sup>. A constant spin of 60 rpm was utilized and a 1° perturbation was established in the  $\phi$  and  $\theta$  directions. The results of the simulation (Fig. 10) were compared to actual telemetered flight data (Fig. 11), where the yaw gyro corresponds to  $\dot{\phi}$ , the pitch gyro corresponds to  $\dot{\theta}$ , and the roll gyro corresponds to  $\dot{\psi}$ . The frequency of the angular-rate oscillations for the simulation matched the 0.5 Hz frequency of oscillation for the STAR 48. A 90° phase shift between the  $\theta$  and  $\phi$  angular rates, present in the simulation, indicated a coning motion. This also agreed with the actual telemetered flight data.

Simulation of the initial test rig design was performed for a five-second time interval. A constant spin of 60 rpm was utilized and a 1° perturbation was established in the  $\phi$  and  $\theta$  directions, where  $I_x = 0.02$ ,  $I_y = 2.37$ , and  $I_z = 2.36$  slug ft<sup>2</sup>. Angular rates vs time are presented in Fig. 12.

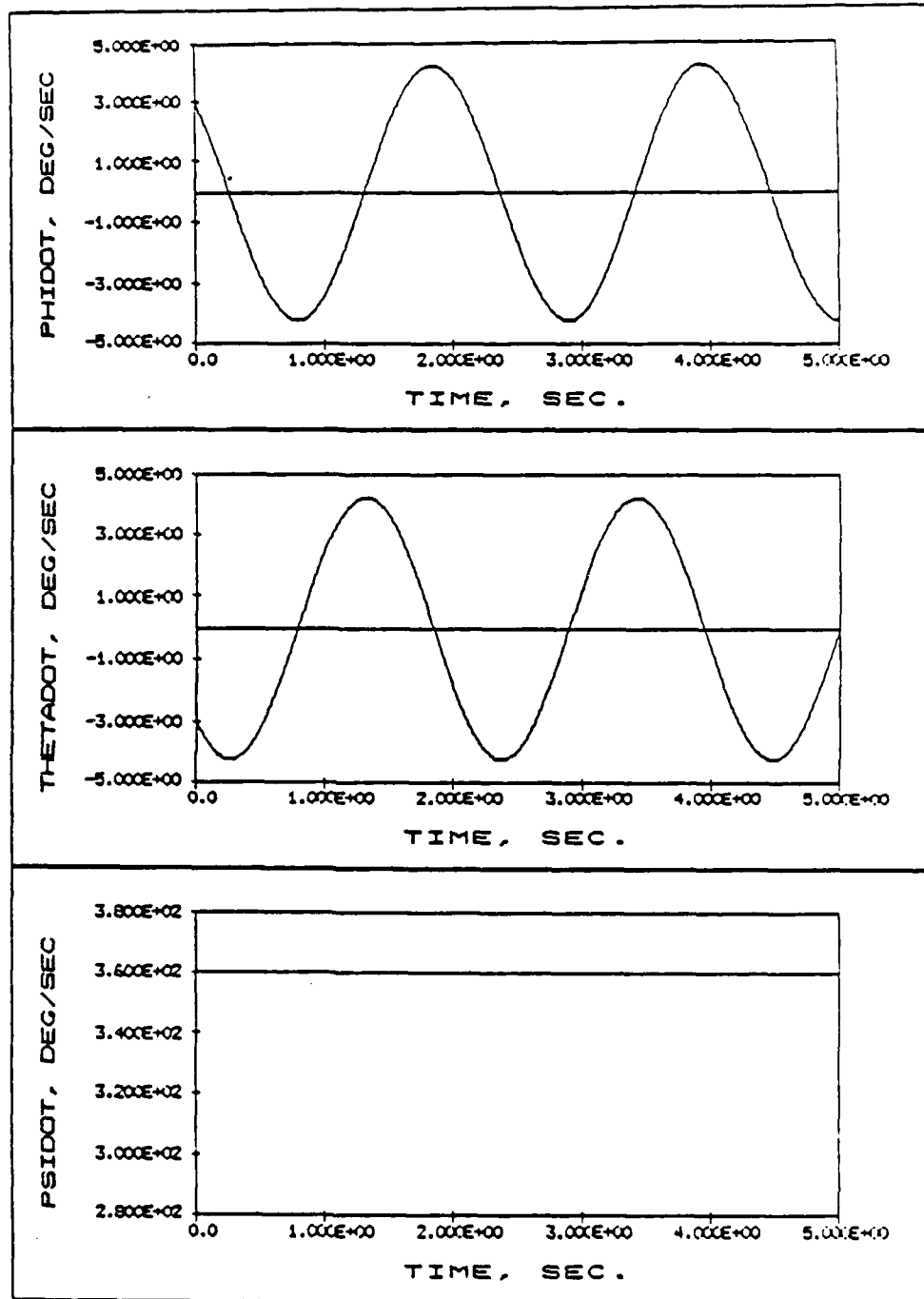


Figure 10. Angular rates vs time for STAR 48, computer simulation.

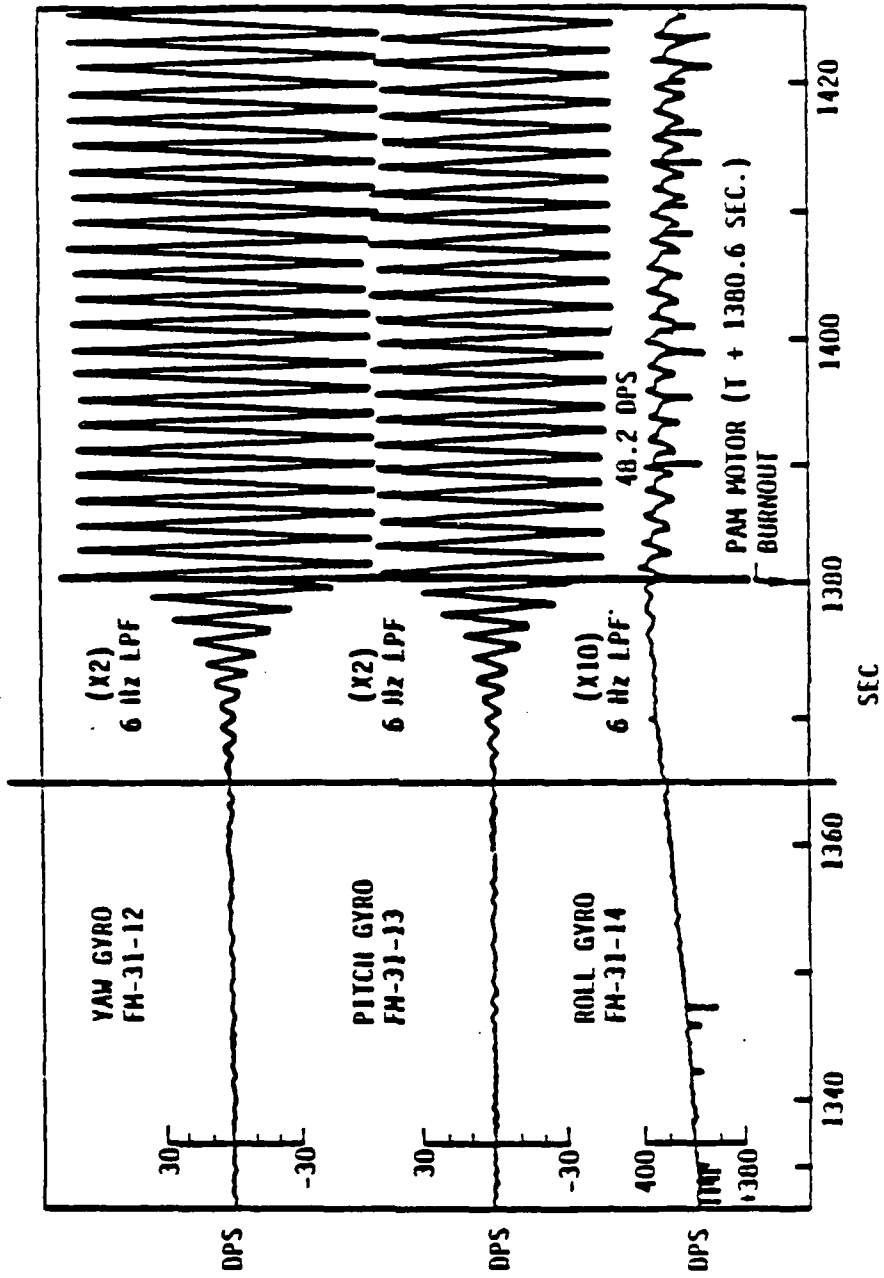


Figure 11. Angular rates vs time for STAR 48, actual telemetered data.

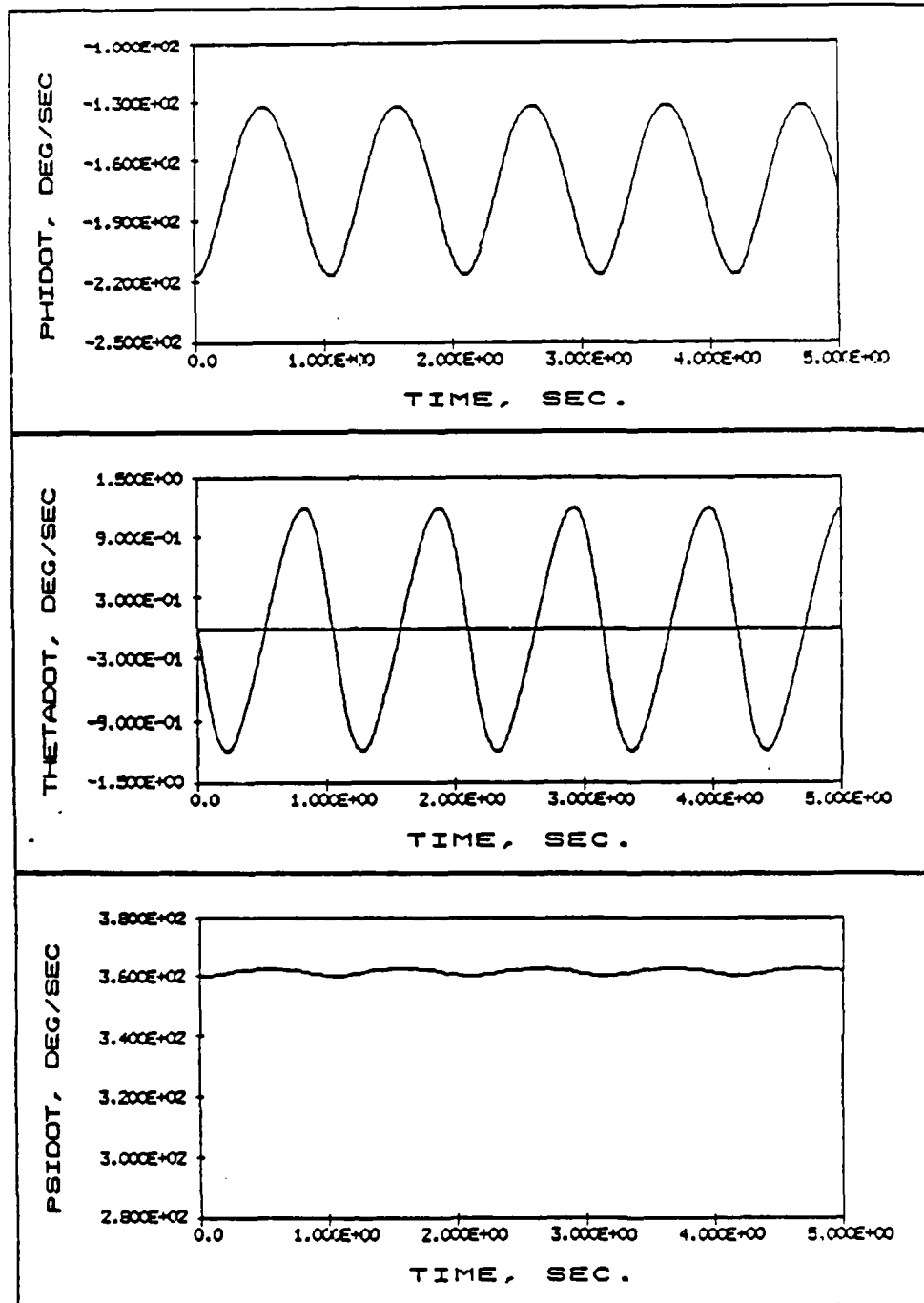


Figure 12. Angular rates vs time for the initial test rig design configuration, computer simulation.

The oscillation of the angular rate of  $\phi$  about a large negative value clearly indicates the instability of this configuration and explains why the test-rig's main supporting cross beam would instantly flop over in the  $\phi$  direction. This can be visualized as the body trying to reorient its spin from the z-axis, the axis of intermediate moment of inertia, to a spin about the y-axis, the axis of maximum moment of inertia.

A computer routine was written to analyze the inertial characteristics of the test rig for various system configurations. Utilizing this routine, we determined that a shorter main support beam of 35.2 in., combined with the addition of a 54.6 in. inertial counter-balance beam normal to the main beam, would result in a maximum moment of inertia about the z-axis and hence a spin about the axis of maximum moment of inertia. The inertias are  $I_x = 0.13$ ,  $I_y = 2.38$ , and  $I_z = 2.46$  slug ft<sup>2</sup>.

The operation of the second design configuration was simulated with the computer software under the same initial conditions as for the first design. Angular rates versus time for the second design are presented in Fig. 13. The oscillation of the  $\dot{\theta}$  and  $\dot{\phi}$  angular rates about zero indicates a marginally stable motion. The simulated angular rates don't converge to zero after they are perturbed because the routine doesn't allow for any energy dissipation. The simulation results can be considered stable since the spin is about the axis of maximum moment of inertia and any real physical system contains energy dissipating elements that would serve to reduce the magnitude of the coning oscillations to zero. One must recall, though, that if the spin were about the axis of minimum moment of inertia, energy dissipation would serve to increase the coning amplitude until the system reached a flat spin—that is, spin about the axis of maximum moment of inertia.

Operation of the second configuration, shown in Fig. 14, proved to be very stable. Any perturbation disappeared within one or two seconds. It was impossible to determine whether any fluid slosh was present and whether there was any interaction between the fluid and the physical structure.

It was decided that a spin about the minimum axis of inertia, a spin that is stable only if there is no internal energy dissipation, would best demonstrate the destabilizing effects of sloshing liquid fuel on a spin-stabilized vehicle.

Because of the physical constraints of the test rig, no configuration with the spin axis as the axis of minimum moment of inertia, and with the system center of mass located at the intersection of the universal joint axes, was possible. It was determined that redesign of the test rig would be required to thoroughly study a torque-free spin about the minimum axis of inertia.

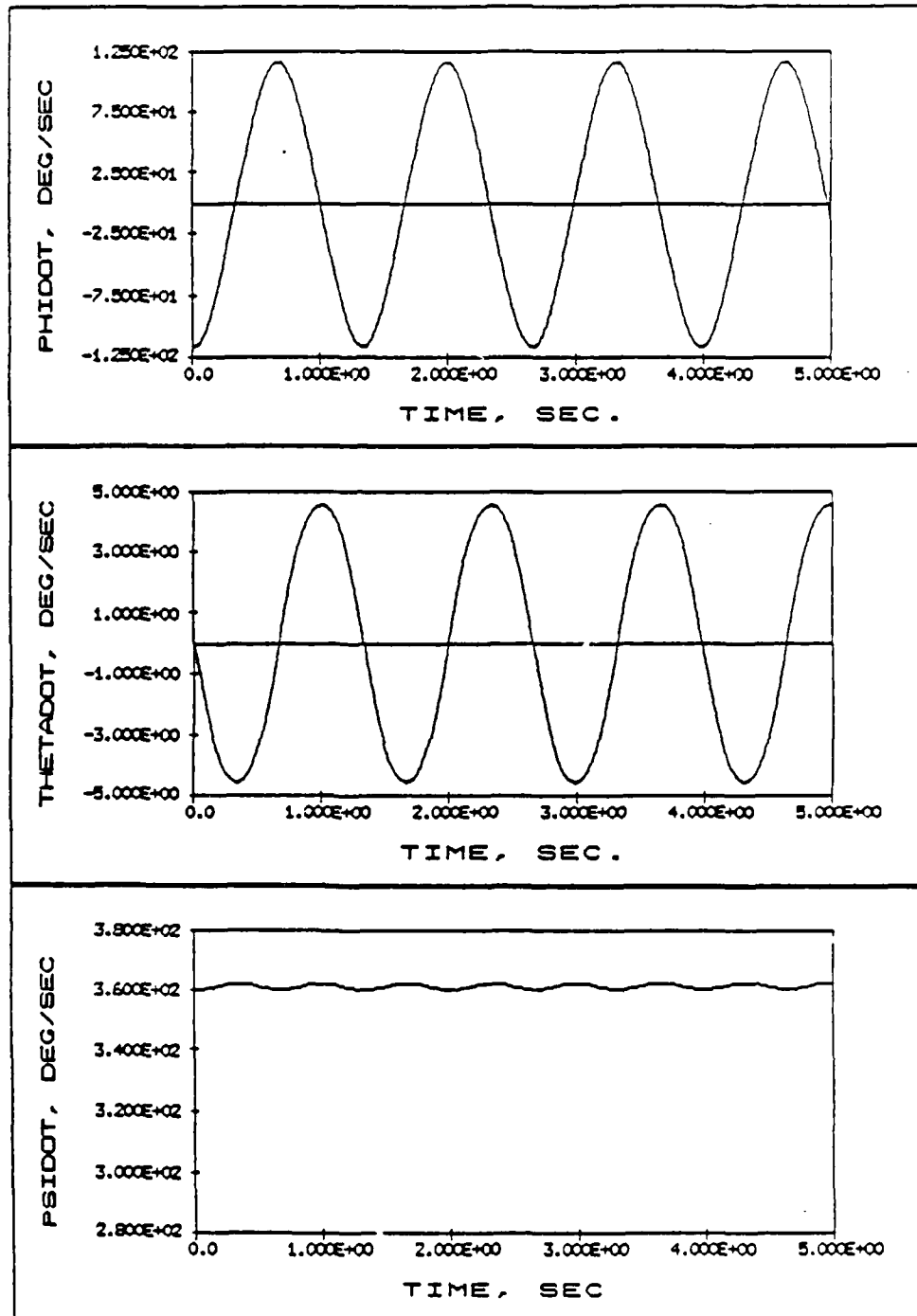


Figure 13. Angular rates vs time for second test rig design configuration, computer simulation.

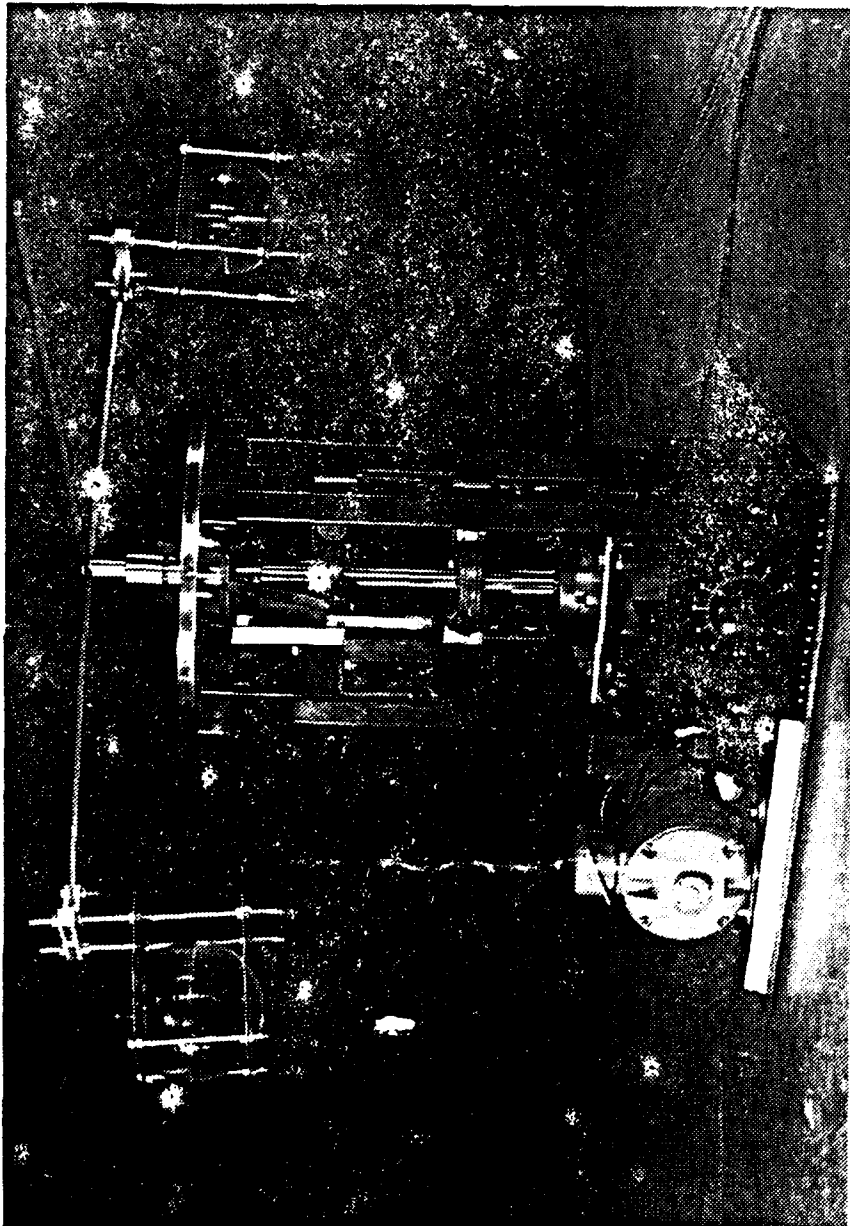


Figure 14. Photograph of completed test rig, second design configuration, spin about axis of maximum moment of inertia.

#### 4. DIMENSIONAL ANALYSIS

In order to maximize the usefulness of the test set-up, principles of dimensional analysis and similitude were applied to the test rig. The results of this effort can be used to design future test rig configurations and to scale test results to obtain predictions of actual STAR 48 satellite motions.

A list of parameters was compiled to describe the system dynamics. The parameters and their respective fundamental dimensions follow:

- $h$  = fluid depth, L
- $\sigma$  = spin to transverse moment of inertia, assuming axisymmetric bodies only,  $I_y/I_x$
- $t$  = time, T
- $\omega$  = initial rate of spin,  $T^{-1}$
- $\theta$  = nutation angle
- $\rho$  = fluid density,  $ML^{-3}$
- $\mu$  = fluid viscosity,  $ML^{-1}T^{-1}$
- $R$  = tank radius, L
- $g$  = gravitational and/or inertial acceleration,  $LT^{-2}$
- $s$  = liquid surface tension,  $MT^{-2}$
- $u$  = displacement of sphere due to transverse beam flex, L
- $k$  = transverse spring rate of support beam,  $MT^{-2}$
- $c$  = effective beam damping in transverse direction,  $MT^{-1}$
- $M$  = ratio of liquid mass to rotating mass
- $F$  = slosh force, response variable,  $MLT^{-2}$

where  $M$  = mass,  $L$  = length, and  $T$  = time.

Inspecting the list of parameters, one finds that many of the terms are already dimensionless. These terms may be considered  $\pi$ -terms to be used for scaling purposes. The first of these terms are

$$\pi_1 = \sigma$$

$$\pi_2 = \theta$$

$$\pi_3 = M$$

All of the remaining parameters are described by the three fundamental dimensions—mass, length, and time. Therefore, the list of parameters can be reduced by three through the use of the "pi theorem."

Because  $\pi$ -terms are products or quotients of the original parameters, and these products or quotients are dimensionless, a general statement of dimensional homogeneity of the original parameters can be formed:

$$F^{a1} c^{a2} \rho^{a3} \mu^{a4} R^{a5} g^{a6} s^{a7} k^{a8} u^{a9} h^{a10} \omega^{a11} t^{a12} \stackrel{d}{=} M^0 L^0 T^0 \quad (38)$$

where the exponential  $a$ 's are integer constants and the equals sign with a "d" over it means "dimensionally equivalent." Step-by-step application of the method yields the following dimensionless  $\pi$ -terms:

$$\begin{aligned} \pi_4 &= \omega t \\ \pi_5 &= F/\rho R^4 \omega^2 \\ \pi_6 &= c/\rho R^3 \omega \\ \pi_7 &= \mu/\rho R^2 \omega \\ \pi_8 &= g/R \omega^2 \\ \pi_9 &= s/\rho R^3 \omega^2 \\ \pi_{10} &= k/\rho R^3 \omega^2 \\ \pi_{11} &= u/R \\ \pi_{12} &= h/R \end{aligned} \quad (39)$$

Many of these terms are identical to those obtained by other researchers of sloshing fluids. By utilizing properties of  $\pi$ -term manipulation, we can modify some of the other terms and find them to be equivalent to the results of others. For example, multiplying  $\pi_7$  by  $(\pi_8)^{-1}$  yields

$$\pi_7 (\pi_8)^{-1} = \frac{\mu}{\rho R^{3/2} g^{1/2}} \quad (40)$$

This term is commonly referred to as the Galileo number. It represents the ratio of viscous effects to gravitational effects. For proper force scaling the Galileo number should be correctly scaled.

$\pi_4$  is known as dimensionless time.

$\pi_5$  is the dimensionless term relating the force response parameter,  $F$ , to the inertial force of the liquid mass. This term can be interpreted as a magnification factor for the fluid slosh force.

The beam spring rate and damping ratio were included in the dimensional analysis for future use when the interaction of the elastic structure and sloshing liquid is considered.  $n$ -terms 10 and 6 should be used to scale beam spring rate and damping ratio.

$n_7$  is commonly known as Stoke's number, relating the viscous effects to inertial effects.

$(n_8)^{-1}$  is known as the Froude number and is the primary scaling factor for the test rig. It indicates the ratio of inertial to gravitational effects. Hence, it indicates the way that gravity should be scaled. Since all frequencies must scale as dictated by the Froude number, we can scale the prototype natural frequency,  $(f_n)_p$ , from the measured model natural frequency,  $(f_n)_m$ , by requiring the Froude number to be the same for the model and prototype:

$$\left( \frac{R(f_n)^2}{g} \right)_p = \left( \frac{R(f_n)^2}{g} \right)_m \quad (41)$$

Rearranging and solving for the prototype natural frequency, one finds

$$(f_n)_p = \left( \frac{(g)_p (R)_m}{(g)_m (R)_p} \right)^{1/2} (f_n)_m \quad (42)$$

Hence, a direct scaling relationship has been determined that relates the frequencies, tank radii, and effective gravitational accelerations between the model and prototype.

Equation (42) may be used to scale frequencies for two modes of free surface fluid slosh. One mode corresponds to oscillations in the vertical or transverse plane, while the other mode corresponds to oscillations in the horizontal or circumferential plane.

For the STAR 48 (prototype), the effective gravitational acceleration is simply the normal component of angular acceleration since the acceleration due to gravity is negligible in orbit. For the test rig (model), the effective gravitational acceleration is approximated by the vector combination of the normal component of angular acceleration and the acceleration due to gravity. Since the two components of acceleration are perpendicular to each other, the magnitude of the effective gravitational acceleration for the test rig can be determined in the following form:

$$g_m = \left\{ \left| r_m (\omega_m)^2 \right|^2 + (g_o)^2 \right\}^{1/2} \quad (43)$$

where  $r_m$  is a characteristic length that depends upon the mode of oscillation as well as the position of the tank center and its liquid contents, and  $g_o$  is the local gravitational acceleration acting in the plane of oscillation. If we utilize Eqs. (42) and (43) it is possible to scale test-rig spin rate, tank radii, and slosh frequencies to or from the STAR 48 spin rate, tank radii, and slosh frequencies:

$$(f_n)_p = \left( \frac{[r_p(\omega_p)]^2 (R)_m}{(R)_p \left\{ [r_m(\omega_m)]^2 + (g_o)^2 \right\}^{1/2}} \right)^{1/2} (f_n)_m \quad (44)$$

where  $r_p$  is defined for the prototype in the same manner as  $r_m$  is defined for the model.

Consideration of the other  $n$ -terms reveals that multiplication of  $n_9$  by  $(n_8)^{-1}$  yields

$$n_9(n_8)^{-1} = \left( \frac{s}{\rho R^2 g} \right) \quad (45)$$

This term is known as the Bond number. It indicates the ratio of surface tension forces to gravitational forces. Generally, the gravitational forces are so large compared to the surface tension forces that the Bond number need not be scaled. Only when  $g$  is very small, as it is for a low-gravity space maneuver of a non-spinning vehicle, is the Bond number an important parameter.

$n$ -terms 11 and 12 are geometric scaling relationships. Term 12 represents the ratio of tank fill height to tank radius and is an integral part of the calculation of fluid slosh resonances.

Theoretically, total similarity between the model and prototype can only be accomplished by satisfying all of the dimensionless  $n$ -terms between the model and prototype. Unfortunately, this can be impossible for some of the terms because of various physical constraints. For example, the Galileo number is very difficult to satisfy because of the small viscosities of most propellants and the large tank radii of most prototypes. Therefore, the modeling of a large tank with a smaller tank could require the use of an exotic or nonexistent fluid. Consequently, researchers must decide which of the terms to satisfy in order to develop an accurate model of the desired physical parameters.

## 5. CURRENT STATUS AND FUTURE GOALS

Presently, work is continuing in three specific directions. Development of the fluid model remains a high-priority effort; redesign and instrumentation of the test rig is nearing completion; and computer simulation of the rotating structure, with the fluid modeled as equivalent pendula, is progressing.

The work on the two-dimensional rectangular model is expected to be completed by the end of January 1988. By that time more data will have been gathered from the inviscid model. Debugging work on the viscous model should be complete and the model expected to yield useful results in the near future. Work on the three-dimensional general model will intensify in early February, and we expect that useful results can be obtained by early summer.

The test rig has been redesigned to raise the universal joint higher above the supporting frame. This will allow the newly modified structure to be rotated about its axis of minimum moment of inertia. Transducers have been obtained to monitor the spin rate of the main vertical shaft, the two-dimensional rotation of the structure with respect to the universal joint, the sloshing of the liquid in the spherical tanks, and the elastic vibration of the rotating structure. All transducers have been mounted on the test rig except for the strain gages, which are to be used to observe the vibrational motion.

The input speed is being measured with a DC generator mounted on the speed reducer between the motor and main vertical shaft. Two potentiometers are used to follow the spatial motion of the rotating assembly relative to the universal joint, and three photo-potentiometers are positioned on each of the transparent spheres to track the location of the liquid surface during test runs. A set of slip rings transfers signals from the rotating member to the computer acquisition system used to record data.

Calibration curves for the various transducers are presently being developed, and different lighting schemes to improve the output from the photo-potentiometers are being evaluated. The strain gages will be added after the initial set of runs with existing instrumentation. The system should be debugged and ready to produce usable experimental results by the beginning of February. Its present status is depicted in Fig. 15.

Meanwhile, two computer models are being developed for simulation of the test rig. A dynamic analysis software package is available locally that will allow the test rig assembly with the fluid replaced by two-dimensional pendula to be described for dynamic analysis without our having to derive the actual equations of motion. Results from this model should be available by mid-February. In addition, the equations of motion are being developed by use of a Lagrangian approach. These will then be solved by one of the differential equation subroutines readily available today. Results from the two computer models will be compared with each other for verification purposes, and they will

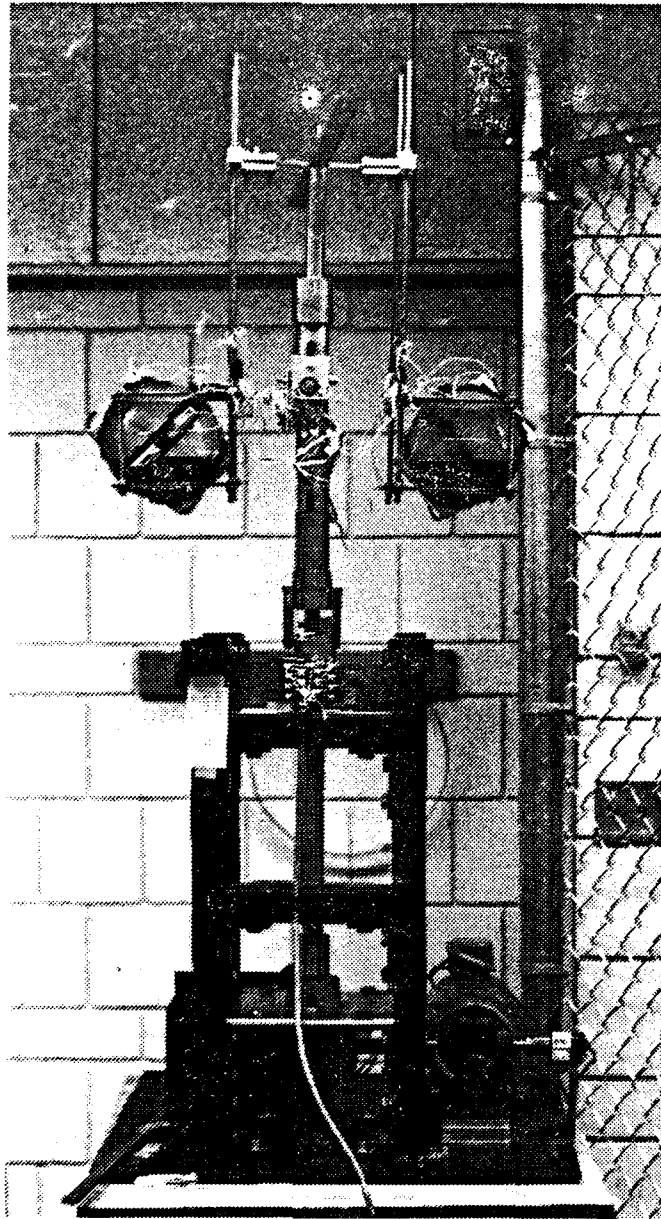


Figure 15. Present test rig with modified design and instrumentation.

also be compared with experimental results. The equivalent pendula will eventually be replaced by the three-dimensional fluid model for simulation purposes.